ARTICLE

Partial substitution of CdS buffer layer with interplay of fullerenes in kesterite solar cells

David Payno[a], Yudania Sánchez[c], Oriol Blázquez[c], Sergio Giraldo[c], Manuel Salado[a], Samrana Kazim[a,b], Edgardo Saucedo [c,d] and Shahzada Ahmad [a,b*]

Over the last decades, significant progress has been made in inorganic materials to enable them as next generation photovoltaic materials that can fulfil the green energy demands. $Cu_2ZnSn(S,Se)_4$ stands out as a p-type absorber material due to exemption from scarce and strategic elements and its similarities with $Cu_2InGa(S,Se)_4$. Organic materials such as fullerenes and its derivatives are effective *n*-type semicondcutors. We report the usage of *n*-type fullerenes materials with kesterite-based absorbers in a thin film polycrystalline solar cell for the partial substitution of the CdS buffer layer with C_{60} or C_{70} fullerenes. Impedance measurements reveals that using C_{60} as an interlayer increases built-in potential, suggesting reduction in the interfacial recombination. This promotes charge conduction, resulting in an increased open circuit voltage and thus device performance.

Introduction

$Cu_2ZnSnSe_4$ (CZTSe) and Cu_2ZnSnS_4 (CZTS) having a kesterite structure are promising absorber materials for large-scale solar integration, due to its unique composition which encompasses of abundant and non-toxic elements. The high absorption coefficient of kesterite facilitate its application in thin films and flexible devices, moreover its tuneable band-gap ranging between 1 – 1.5 eV is suitable for single junction solar cells. Furthermore, they exhibit robust stability in outdoor conditions[1]. The potential of being solution processable makes it attractive for small scale manufacturing and low capital cost[2]. However, the advancement in Kesterite has been impeded and was subject to less exploitation during last years owing to its complexity and relatively low power conversion efficiency (PCE) as compared to the other thin film emerging photovoltaic technologies[3]. One of the reasons for the lower performance lies in the formation of the junction with the buffer layer[4]. Unfavourable band alignment, dipole formation and lattice mismatch creates recombination paths that lowers the open-circuit voltage. Further, buffer layers absorbs part of the solar spectrum, which reduces the short-circuit current. CdS is the most studied *n*-type buffer layer for thin film solar cells, inherited from the established technologies such as CdTe and $Cu_2InGaSe_4$ (CIGS), where it gave competitive PCE, owing to its

high transparency, electrical properties and ease of processing through chemical bath deposition (CBD)[4–6]. Attempts to modify or substitute this buffer layer was limited to Zn(S,O) [7–9], In_2S_3 [10], (Zn,Sn)O [11], (Cd,Zn)S[12] or alloys with CdS[12,13]. However, little improvements in terms of reproducibility were obtained. In most of the cases, a second *n*-type material is required to improve the charge conduction and to minimize short circuits, typically ZnO as window layer.

On the other hand, organic semiconductors have delivered significant results, due to the tuneable electro-optical properties that can be achieved by engineering the molecules. Fullerenes are being employed since 1985[14], and their photovoltaic properties are studied[15,16]. Currently, fullerenes and its derivatives are widely used in organic and perovskite based solar cells, as an electron transport materials to achieve high performance[17–19]. They are environmental friendly and stable, as they are composed of carbon atoms joined by covalent bonds. They can be further functionalized to increase its solubility, as in the case of [*6,6*]-phenyl-C_{61}-butyric acid methyl ester (PCBM).

However, reports dealing with fullerenes in kesterite solar cells are in scarce and limited efforts were made of combining CZTSSe with organic materials. CZTSSe nanocrystals have been used for photodetectors or improvements in organic solar cells.[20–22] Among the reports, Saha *et al* made attempt to create a planar superstrate device with CZTS nanoparticles and PCBM, with the limitation of having a non-ohmic contact between ITO and CZTS[22], measuring 0.9% PCE. Jang et al introduced CZTS nanoparticles into a bulk heterojunction (P3HT:PCBM) to improve the absorption of the organic solar cell, thus increasing the generated photocurrent and yielding a PCE of 3.32%[21]. Nevertheless, these attempts exhibited poor photovoltaic performances.

In this work, we designed an architect for both kesterite (CZTS and CZTSe) based absorbers, by the introduction of *n*-type C_{60}

a. *BCMaterials, Basque Center for Materials, Applications and Nanostructures, Bld. Martina Casiano, UPV/EHU Science Park, Barrio Sarriena s/n, 48940 Leioa, Spain Tel: +34 946128811 Email:shahzada.ahmad@bcmaterials.net*

b. *IKERBASQUE, Basque Foundation for Science, Bilbao, 48013, Spain*

c. *Catalonia Institute for Energy Research (IREC), Jardin de les Dones de Negre 1, 08930 Sant Adrià de Besòs, Barcelona, Spain.*

d. *Department of Electronic Engineering, Polytechnic University of Catalonia (UPC), Sor Eulàlia d'Anzizu 6, 08034 Barcelona, Spain.*

and C_{70} fullerenes as interlayer and reducing the CdS thickness. The reduction of CdS thickness was found to be advantageous by many groups, due to higher transparency in the short wavelength region and low series resistance, additionally, owing to the reduced loadings of the highly contaminant and toxic Cd. On the contrary, reduced CdS thickness resulted into lower voltage and high risk of pinholes[23,24], an effect that is more remarkable in CZTS than in CZTSe[25].

We settled for the best possible configuration of a bilayer buffer by changing the deposition order, and put forward promising results for both absorbers with C_{60}. The measured open circuit voltage are notably high with both type of absorbers and gave a PCE of 8.37% and 4.58% with CZTSe and CZTS respectively, even with reduce thickness of CdS. Additionally, an array of electrical measurements (impedance and *C-V*) were made for the CZTS samples to observe underlying phenomena. An increase in built in potential (V_{bi}) and a reduction in the interface recombination was noted, allowing a significant improvement in the charge transport.

Experimental method

Device

For the fabrication of CZTSe and CZTS solar cells, a cleaned soda-lime glass (SLG) were used as substrate providing sodium (Na) source. 800 nm thick film of Molybdenum (Mo) was sputtered on the SLG as back contact, followed by the deposition of metallic precursors Sn, Cu and Zn. For the selenium containing absorbers, also a thin film of 20nm of Ge was deposited by the thermal evaporation, as a doping agent to improve bulk quality[26,27]. This was then placed into a closed graphite box, and then introduced inside a quartz tube furnace to perform the sulfurization or selenization. The annealing treatment was performed in two steps, in a first step, low temperature was used to create the sulphides or selenides binary compounds, and in a second step high temperature treatment was made to form the quaternary compound and to promote the grain growth.

An etching treatment was performed by dipping the samples in a 22% diluted $(NH_4)_2S$ in H_2O, in order to remove the binary $Sn(S,Se)_x$ compounds formed at the interface. An extra air annealing treatment of 300°C was applied to the CZTS absorber to oxidize some of the remaining binary compounds.

The following buffer layers were deposited on top of the absorber. CdS was grown by chemical bath deposition (CBD). $Cd(NO_3)_2$ was used as Cd precursor for CdS in the CBD, which allows a better growth control of the thickness as the formation is slower[28]. For standard deposition, 60 nm film grown in 40 minutes duration was required to achieve the best performance[23,29], however, notably in this work, the process was reduced to 20 minutes in order to minimize the thickness, producing a thinner film of ~30nm of CdS. The fullerenes C_{60} and C_{70} thin films were prepared following the procedure reported elsewhere[18]. The fullerenes were dissolved with a concentration of 10mg/mL in 1,2-dichlorobenzene and keeping it stirring overnight. The solution was filtered with a PTFE filter of 0.42 μm pore size, and deposited by spin coating 50 μL at

1500 rpm for 60 seconds. After spin coating, it was transferred on a hotplate to dry at 80°C for 2 minutes. The devices were finished by sputtering 50nm of ZnO as a window layer and 300nm of ITO as transparent conductive film at 200°C. Further, neither top metallic contact nor anti-reflection coating was used in this work. The cells were then mechanically scribed in squares of 3x3 mm^2.

Characterization

Absorption and transmittance spectre were recorded with the help of Agilent Cary 60 UV-Vis spectrometer. For the device characterization, the current-voltage curves were measured using a class AAA Oriel solar simulator from Newport and a Keithley multi-meter, by connecting the positive contact to the bare molybdenum and the negative contact directly to the ITO. The external quantum efficiency (EQE) was measured from 300 – 1100 nm range on a PVE300 Photovoltaic EQE system, powered by a 150W Xenon lamp and a 1/4m monochromator. For the impedance measurements, a constant bias signal with 20mV of perturbation was applied, in a frequency range from 5GHz – 300Hz. The measurements were made inside a Faraday chamber, to avoid signal interferences, using Biologic impedance analyser and EC-LAB software was used for fitting of the data to extract the parameters of the equivalent circuit.

Results and discussion

Optical characterization

A prerequisite of a buffer layer is high transmittance in a wide range of both visible and near infrared wavelengths, in order to allow the maximum light absorption by active material. The optical properties were acquired on the films deposited on glass (*Fig.1)*. Transmittance spectra of the CdS thin films with a thickness of 30-40 nm exhibits higher transparency from 450-1000 nm wavelength, while for the thickness of 60-70 nm, further 15-20% of the transmittance is reduced in the same wavelength region for CdS, and further decreased for annealed film of CdS in the wavelengths smaller than 450nm (Fig.1a).

To unravel the effect of annealing on the band gap of buffer layer, the film was annealed at 230°C for 20 min in air and transmittance was measured before and after to calculate the optical band gap by Tauc plot method (Fig.S1a). Besides the reduction in the transmittance in the 480-580 nm range, the annealed film of CdS also exhibits a red shifting in the band-gap from 2.35eV to 2.23eV (*Fig. S1a)*. This change is associated with a transition from hexagonal to cubic structure and in case of C_{60}, the minute loss in transmittance occurs at 500nm, while in case of C_{70}, it shows slight loss in transparency from 450 to 700nm. Thus, the high optical transparency of these organic materials suggest its usage as buffer layer with a low band-gap absorber material such as kesterite.

However, parasitic absorption of these materials can slightly reduce the photocurrent that will be higher in the case of C_{70}. The calculated optical band-gaps of these fullerenes through a linear fit of the tauc plot (Figure S1b) and the values are in agreement with reported value in the literature.
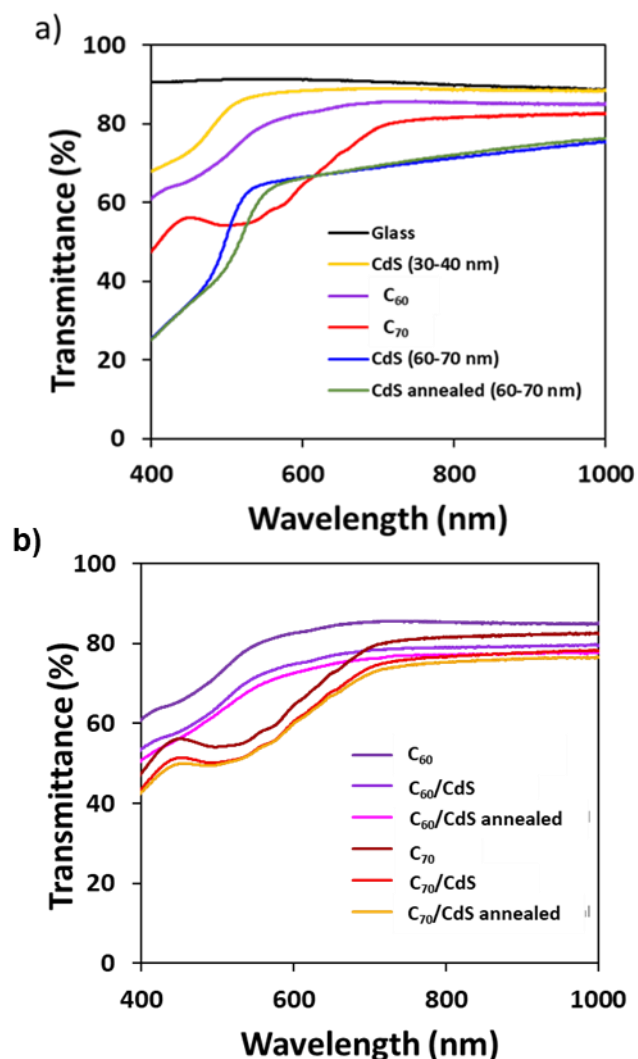
Figure 1. a) Transmittance spectra of thin films deposited on glass of C_{60} , C_{70} (spin coating) and CdS (CBD) and b) transmittance spectra of the bilayer buffer before and after heat treatment of 230°C for 20 mins.

Fig.1b shows the changes in transmittance of the C_{60} and C_{70} films after the deposition of CdS thin film, and after annealing in air at 230°C for 20 mins. In both cases, the trend is similar, however, a reduction of 5-10% of the transmittance can be observed after the organic material is covered with CdS, and an unnoticeable reduction in the transmittance after the heat treatment. No changes in the bandgap are noted suggesting the amorphous nature of the fullerenes is conserved.

Fig.2 illustrates the energy levels diagram of the studied device with the employed materials. In spite of different band-gaps of the materials, the energy level of the LUMO is close to the conduction band of the CZTS(e) in all cases, which facilitates the flow of electrons while the low energy level of the HOMO can block the holes effectively, making it ideal candidates as buffer layer.
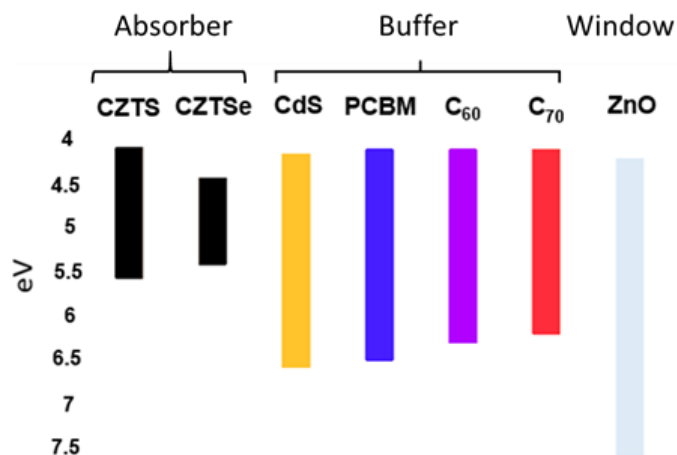
Figure 2. Energy level diagram of the architect used (PCBM can be found in supporting information

Device characterization

Firstly, we have employed CZTSe as an absorber layer. Three different configurations were prepared (*Fig.3)* where thickness of CdS is reduced and partially substituted by a fullerene in a double buffer layer. The first one is denoted as CdS/C_{60}. In a second configuration, CdS/C_{70} was probed as buffer film. In a third one, C_{60}/CdS was used as interfacial agent, to test the possibility of minimizing the interface recombination by fullerenes being deposited directly over the CZTSe absorber (shown in the right side of the figure).

The influence of the thickness and the applied heat treatments to CdS on the solar cell performance has been studied. In case of selenium containing absorber, a thin CdS film of 30-50 nm is deposited and a post heat treatment (PHT) above 200°C is applied. This treatment induces a Cd^{2+} diffusion to the absorber, and exchanges between S and Se, reducing the interface recombination and thus improving the voltage and FF. This process was reported for CIGS[30], and is also applied to CZTSe to deliver similar results[31,32].

However, organic materials are susceptible to thermal treatments and can decomposed or oxidized at higher temperature. Decomposition is not an issue for fullerenes as the covalent bonds of the carbon are extremely stable[33]. Further, we have not observe any thermally evaporation of organic materials for temperatures lower than 350°C, in agreement with the transmittance measurements. However, it is vital to evaluate the role of organic layers under the required treatments and the possible effects this may impose in the fabricated solar cell, such as changes in the crystal structure or oxidation may occur.

To evaluate this, the final devices were characterized before and after heat treatment of 230°C for 20 minutes in air on a hotplate. The average parameters extracted from the *J-V* characterization of eight different cells are shown in the *Table 1*. Similar trend was noted for all the devices with C_{60}. The V_{oc} and the FF showed an increased value after the heat treatment, and gave an average PCE >7.5%. In the case of C_{70}, an improvement of the V_{oc} and J_{sc} can be noticed after the heat

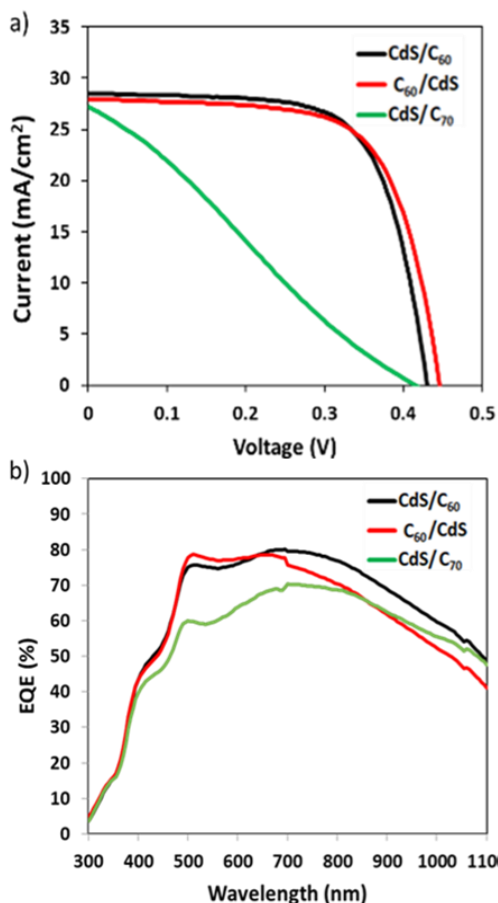treatment, but the reduction in FF resulted in a drop in the final PCE.
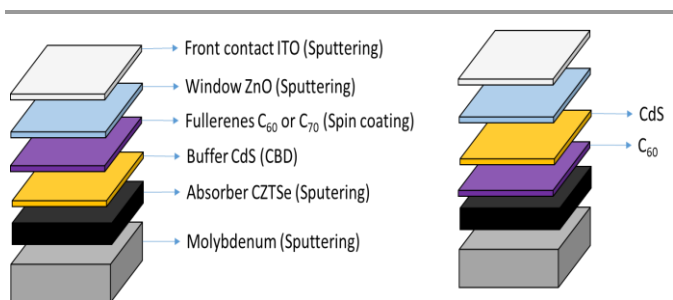
Figure 2. Architecture of the different configurations of kesterites used for solar cells fabrication.

Table 1. Standard deviation of eight cells before and after the post heat treatment.

Type	Heat treatment	V_{oc} (mV)	J_{sc} (mA/cm²)	FF (%)	PCE (%)
CdS/C$_{60}$	As prepared	404 ± 5	26.00 ± 0.80	49.2 ± 2.1	5.16 ± 0.3
	After PHT	423 ± 8	27.91 ± 0.73	63.7 ± 3.5	7.54 ± 0.7
C$_{60}$/CdS	As prepared	338 ± 34	24.24 ± 2.2	41.0 ± 5.6	3.45 ± 1.1
	After PHT	443 ± 6	27.21 ± 0.57	64.0 ± 2.9	7.72 ± 0.4
CdS/C$_{70}$	As prepared	404 ± 6	19.62 ± 0.80	31.7 ± 1.1	2.52 ± 0.1
	After PHT	416 ± 2	22.85 ± 2.4	21.8 ± 3.1	2.09 ± 0.5

Figure 3. a) *J-V* curves under 1 sun illumination for CZTSe absorber and b) EQE spectra of the best devices after the post heat treatment.

Table S1 illustrates a detailed study of post heat treatment and suggests the optimized results, with a treatment at 225°C. The open circuit voltage can be further increased at higher temperatures, but a reduction of the current and FF will reduce the PCE. We can speculate that the use of organic layer is compatible with the required post heating treatments and will not hinder the element diffusion between CdS and CZTSe.

The devices using C$_{60}$ between CZTSe and CdS registered 20 mV higher V_{oc} and competitive FF of 64% in average, that can indicate surface passivation effect, but with a minute loss in photocurrent. The *J-V* curves (*Fig.4a)* of the best devices with post heat treatment yielded a value of 446mV of V_{oc}, without compromising other parameters, and a PCE of 8.37% was noted for the champion device. The CdS/C$_{60}$ also showed a similar value and PCE of 8.35% was obtained, due to a slightly higher photocurrent, but a reduced voltage. Samples with a complete substitution of CdS by C$_{60}$ and PCBM (Fig.S3a) was not able to deliver respected performance in comparison with a standard cell using only CdS or bilayer buffer. The external quantum efficiency (EQE) spectra of the devices (Fig. 4b), reveals that the loss of current is higher in the infrared region, which we assigned to the absorber layer itself rather than the buffer or the interfacial layers.

Complementary to this, a higher response in the violet and ultraviolet region can be noticed (*Fig. S3b)*, which can be attributed to a lower parasitic absorption of the double buffer layer in this region in comparison with a pure CdS buffer layer. On the other hand, a loss of response can be noticed in the infrared region for the double buffer films, which is also responsible for the current loss from the ideal value. While the drop in the infrared region is characteristic for CZTSe absorbers, and can be attributed to bulk defects that cause fast recombination of electron-hole pairs produced from the *p-n* junction. We observed slightly lower photocurrent for the double buffers in comparison with only CdS film, which can be attributed to the loss of transparency. For the sample using C$_{70}$, a drop in the *FF* led to a lower PCE than of C$_{60}$. The V_{oc} remains similar, but there is a drop in the current value, as it was expected by transmittance data, and also supported by the EQE measurement, where the signal is reduced for wavelengths shorter than the calculated bandgap (1.79 eV or 700nm). This behaviour is similar to the results of using C$_{70}$ as buffer layer in other type of solar cells[34]. The competitive FF of both CdS/C$_{60}$ and C$_{60}$/CdS suggests rational energy level alignment between the conduction band of CdS and lowest unoccupied molecular orbitals (LUMO) level of C$_{60}$.
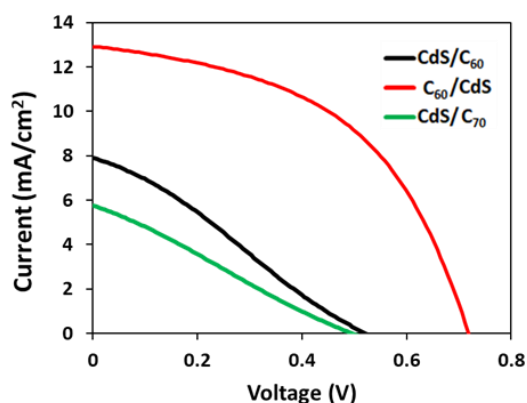
Figure 5. J-V curves of the best device using CZTS as absorber.

Table 2. Averages of the extracted parameters for each configuration with standard deviation

Condition	V_{oc} (mV)	J_{sc} (mA/cm^2)	FF (%)	PCE (%)
CdS/C$_{60}$	520 ± 8	7.5 ± 0.17	27.8 ± 0.6	1.09 ± 0.05
C$_{60}$/CdS	700 ± 32	12.6 ± 0.51	46.7 ± 2.9	4.16 ± 0.54
CdS/C$_{70}$	460 ± 47	5.3 ± 0.33	27.0 ± 1.0	0.65 ± 0.07

The flow of current shows low resistance independently of the layers order, but this is not the case for C$_{70}$ where the low FF indicates a high resistance of the CdS/C$_{70}$ film. Further, these fullerenes were also tested with CZTS absorber, using the similar three configurations as shown in Figure 2. In this case, the surface passivation of the absorber is of significant interest, as the interface between CZTS and CdS presents several issues due to the valence band offset and secondary phases which induces interface recombination. Usually, an etching treatment[35,36] or an oxide interlayer[37,38] is required for a passivation of interface defects.

Fig. 5 shows the *J-V* curves of the best device for each condition under AM1.5 illumination condition, and the average values are shown in the Table 2. In case where C$_{60}$ was used as interlayer between the CZTS absorber and CdS, the devices registered a significant increase in PCE from 1% to 4.5%, with a remarkable V_{oc} of 718 mV in the best cell. Considering that the record value is 730mV for a pure CZTS absorber was achieved by a high temperature thermal annealing and a protective Al$_2$O$_3$ film in the back contact[39]. In this case, no special treatment was applied to the Molybdenum, so an excess of MoS$_2$ formation during the sulfurization could increase the resistance and is responsible for the low FF in these devices.

The EQE spectra (Fig. 6a) was recorded to investigate the deficiency of the current. No relevant changes in the band-gap of the absorber was noticed, having a value of 1.47eV for all cases. The spectra of the CdS/C$_{70}$ sample is losing part of the signal in the 380 – 700 nm region, which can be associated again to the absorption of C$_{70}$ in this region. However, the differences between the samples are lesser than expected from the *J-V* and integrated photocurrent from the EQE is calculated (*Fig.6b)*.
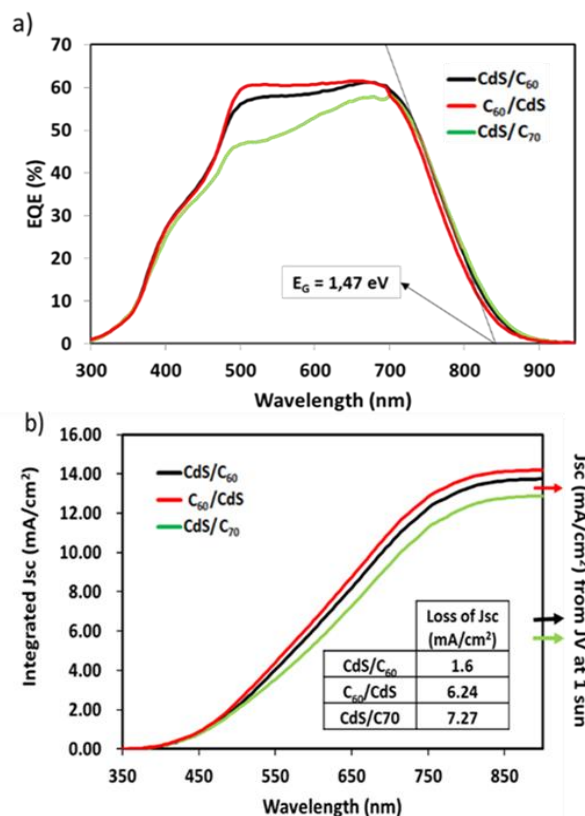

Figure 6. a) EQE spectra of the CZTS samples. The band-gap is calculated in the graph by a linear fitting of the last part of the graph and b) Corresponding integrated photocurrent density extracted from the EQE measurements. The inset table shows the difference between the integrated photocurrent and the J_{sc} measured at 1 sun (marked with an arrow on the right).

The integrated current density value should match with the J_{sc} value measured on *J-V* curve but a difference of 6.24 and 7.27 mA/cm^2 was noted for the samples CdS/C$_{60}$ and CdS/C$_{70}$ respectively. This result reveals that there is a loss of photocurrent when they are illuminated under AM1.5 conditions, effect that is less noticed in the C$_{60}$/CdS sample.

This suggests change in the carrier concentration under light illumination, and a possible high density of defects or secondary phases in the CZTS/CdS interface that can aggravate the accumulation and recombination of the charge in the interface. It seems contradictory to attribute the reduction of the FF to the bilayer buffer, because in the case of C$_{60}$, it works efficiently in the structure of CZTSe/CdS/C$_{60}$. Therefore, we attribute this increase of the resistance to an un-optimized CZTS/CdS interface, and when the C$_{60}$ is placed between CZTS and CdS, the electrons are transported efficiently through the buffer layer and the interface recombination is avoided.

Impedance spectroscopy

Impedance measurements were performed on the devices with a configuration of CZTS/CdS/C$_{60}$ and CZTS/C$_{60}$/CdS to elucidate the role of junction formed. The capacitance measurement at different frequencies can display the behaviour of physical mechanisms occurring at different time scales.
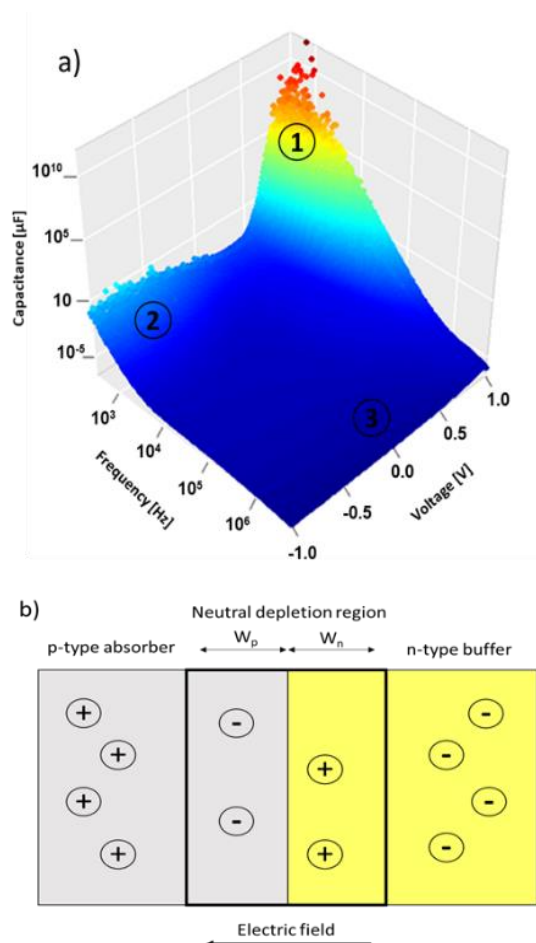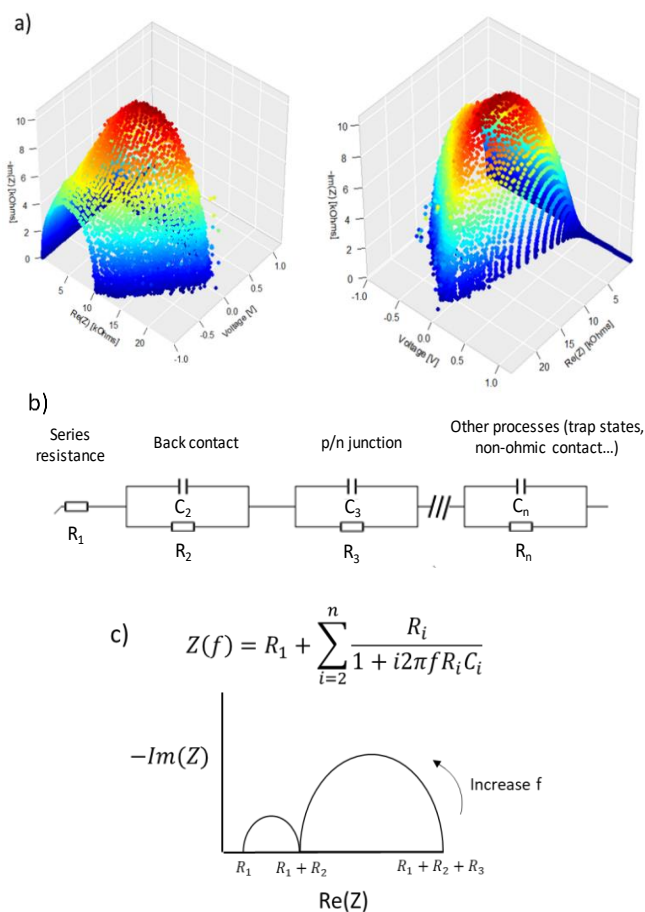
Figure 7. a) Capacitance mapping from a RC circuit vs frequency and voltage, measured under dark, with the three mentioned regions marked and b) scheme of the charges in the p-n junction.

Figure 8. a) Map of the Nyquist plot vs bias voltage with different view perspectives measured in dark, b) equivalent circuit used to fitting the solar cells and c) equation that describes the equivalent circuit for n loops and representation scheme for *n*=3.

While the change of the applied voltage will modify carrier density and the space charge region. 3D mapping of the capacitance from a simple RC circuit is represented in the *Fig.7a*. The capacitance contribution mainly originates from the pseudo-capacitor formed by the *p-n* junction between the absorber and the buffer layer, represented in the scheme (*Fig.7b*). Three main features can be distinguished, marked as 1, 2 and 3 in the *fig7a*:

i) At lower frequencies of 10^2–10^4 Hz, the capacitance rapidly increases with the increment of the direct voltage. While the capacitance is inversely proportional to the width of the depletion region according to the (*Eq.1*) of a capacitor, the width of the depletion region at this point is minimum. For an applied voltage higher than built-in potential, the *p-n* junction allows pass of the current and the capacitance is dominated by the minority carrier diffusion, which is proportional to the current, as shown in the *(Eq.2).* This region is associated with the chemical capacitance.

$$C = \varepsilon_0 \varepsilon_r \frac{A}{W} \tag{1}$$

C is the capacitance, ε_0 the vacuum permittivity, ε_r the relative permittivity, A is the area of the cell and W the depletion width.

$$C_d = I \frac{\tau_T}{V} = \frac{\tau_T}{R} \tag{2}$$

C_d is the diffusion capacitance, I is the current, τ_T is the transit time, V is the applied bias and R the equivalent resistance.

ii) When the applied bias is smaller than the built-in potential, the width of the depletion region is narrowed within the voltage, following the (*Eq.3*). Typically, the buffer layer required a high-density carrier concentration $N_D \gg N_A$, so most of the depletion width falls into the absorber and the equation can be simplified as in the (*eq.4*). At negative bias, the polarization is inverted and the current is blocked, thus the diffusion capacitance is negligible and the charge drift dominates the capacitance, called depletion region capacitance.

$$W_{p \lor n} = \sqrt{\frac{2\varepsilon_0 \varepsilon_s}{q(N_D + N_A)} \frac{N_{D \lor A}}{N_{A \lor D}} (V_{bi} - V)} \tag{3}$$
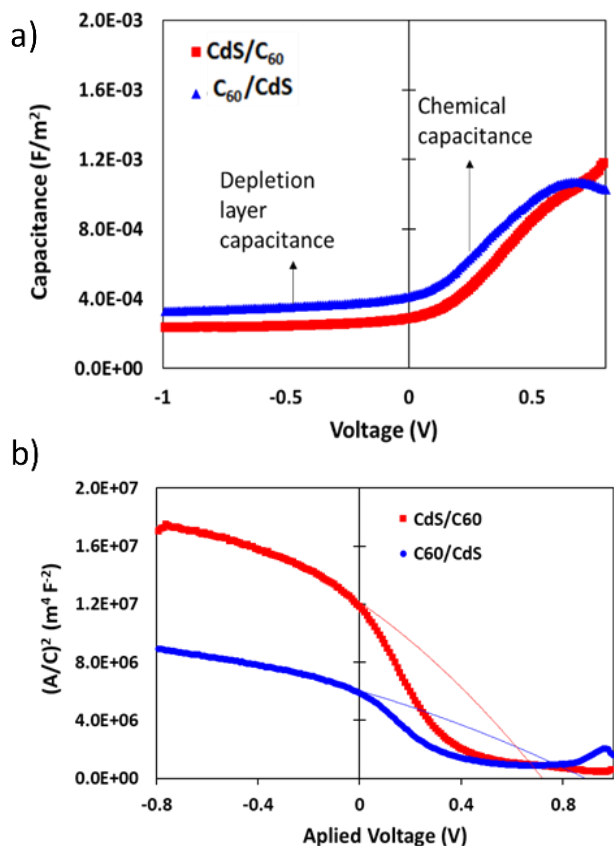
a)

b)

Figure 9. a) Capacitance C3 fitted from the impedance curves vs the applied voltage and b) Mott-Schottky plot with a polynomic fit of the negative voltage.

$$W = W_p + W_n = \sqrt{\frac{2\varepsilon_0\varepsilon_s}{q}\frac{N_D+N_A}{N_D N_A}(V_{bi}-V)} \approx \sqrt{\frac{2\varepsilon_0\varepsilon_s}{qN_a}(V_{bi}-V)} \quad (4)$$

W_p and W_n are the width of the depletion region in the p and n material respectively, ε_s is the relative permittivity, N_D is the donor concentration in the n material, N_A is the acceptor concentration of the p material, V_b is the built-in potential.

iii) At high frequency, the transit time τ_T is much larger than the signal and the charges has no sufficient time to transfer across the device, provoking a drop in the capacitance. At this region, the single effect remaining is the series resistance.

A solar cell is a complex circuit, where many simultaneous processes occurred, thus a simple RC circuit will not be able to provide reliable information. To further expand this, we made fitting in an equivalent circuit to the Nyquist plot. Nyquist plot versus voltage map (Fig. 8a) represents semicircles for which size changes with the voltage. These semicircles fits with equivalent circuit composed by a series resistance followed by a certain number of loops with a capacitor and a resistance[40,41], as illustrated in the *Fig.8b*. Each loop represents a physical process occurring inside the devices. This part is very tricky, as some of the semicircles can be overlapped, making the analysis complex.

The first semicircle is usually associated with the junction p⁺/p in the back contact with the MoS(e)$_2$, while the main semicircle is associated with the *p-n* junction.
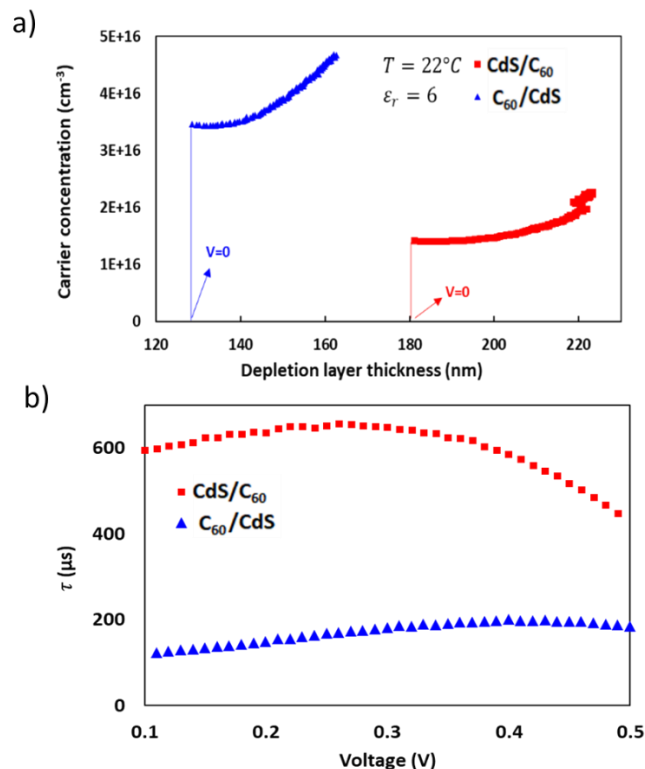
a)

b)

Figure 10. a) Profiling of the calculated donor concentration and b) minority carrier lifetime at different applied bias.

Other processes as trap states or grain boundaries is generally overlapped with the main semicircle, producing a modification in the shape. These semicircles are ideally described as the scheme showed in *Fig.8c*. By minimizing the error between the equivalent circuit and the measurement, different values of the capacitance and resistance can be extracted for different processes, independently from the frequency. The value of C$_3$ is represented in the *Fig.9a* for the CZTS absorber using (CZTS/C$_{60}$/CdS and CZTS/CdS/C$_6$)$_0$ configuration. Two different regions can be clearly differentiated, as in the R$_C$ circuit of the Fig.7a, at negative voltage the capacitance is dominated by the depletion layer, while at sufficient forward voltage, the capacitance is dominated by the chemical capacitance. From the value of the capacitance C$_3$, which represent *p-n* junction at reverse voltage, a Mott-Schottky plot can be determined by plotting (Area/C$_3$)^2 vs applied voltage, illustrated in the Fig.9b. Typically, the built-in voltage can be calculated by the intercepting the x axis to a linear fit at reverse voltage because this is the region where the capacitance is dominated by the pseudocapacitor of the depletion layer.[42] However, here it does not follow a linear trend, and fits well with a second order polynomial. This is a characteristic behaviour of non-crystalline and polycrystalline materials, which indicates the presence of non-ideal processes such as deep levels. Therefore, the built-in potential is calculated by the extrapolation of the polynomial fit to the cross with the x axis, and a term of kT/q is substracted.
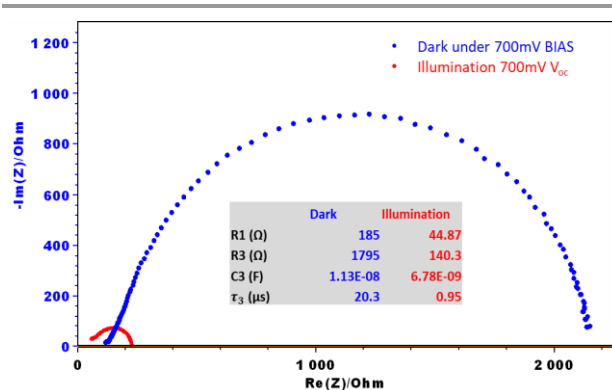
Figure 4. Impedance spectra under illumination (white LED), having 700mV of V_{oc}, and in dark on an applied bias of 700mV. The parameters of fit with n=3 are showed in the table inside.

Table 2. Calculated parameters from C-V measurements at V = 0V, in dark. τ_T is measured at V = 0.3V.

Device configuration	V_{bi} (V)	N_A (cm^{-3})	W (nm)	τ_T (µS)
CZTS/CdS/C$_{60}$	0.709	1.41× 1016	183	647.2
CZTS/C$_{60}$/CdS	0.864	3.47 ×1016	128	181.3

From Table 3, we can deduct a significant increase in the built-in voltage of 155 mV for the sample CZTS/C$_{60}$/CdS, pointing towards the increase of V_{oc} in these solar cells. This increase of $\boldsymbol{V_{bi}}$ can be associated with a higher voltage in the depletion region, which will contribute to the final V_{oc}.

By elucidating the $\boldsymbol{V_{bi}}$ value, a representation of the carrier concentration in the absorber can be calculated by the (Eq.5), using the same criteria $N_D \gg N_A$ (Eq.6). While N$_A$ is usually reported in the order of 10^{16} cm^{-3} for CZTS, N$_D$ for both CdS and C$_{60}$ has been reported in the order of 10^{18}cm^{-3}. Carrier concentration versus depletion width is represented in the *Fig. 9a*, where the width is calculated by the (*Eq.1*). It can be noted that the depletion width is broader and the carrier density is lower for the CZTS/CdS/C$_{60}$ based device.

The C$_{60}$ employed as buffer layer increases the apparent carrier concentration of the CZTS close to the interface, which may indicate a passivation of the CZTS surface by preventing the surface recombination. On the other hand, the reduction in the depletion width is about 55nm. However, this reduction is not desirable, as it may not affect if the diffusion length of the photo-generated charge is at least in the order of the thickness of the absorber, so all the charge can reach the space charge region.

An analogue situation has been reported for the use of an In$_2$S$_3$ interlayer between CZTS and CdS, where a similar effect of increased carrier concentration and reduction of the interlayer was found, resulted in an improved open circuit-voltage.[43]

$$\frac{A^2}{C^2} = \frac{2}{q\,\varepsilon_0\,\varepsilon_{buffer}\,\varepsilon_{CZTS}}\frac{N_D\varepsilon_{buffer}+N_A\varepsilon_{CZTS}}{N_D\,N_A}(V_{bi}-V) \qquad (5)$$

$$\frac{A^2}{C^2} \stackrel{N_D \gg N_A}{\approx} \frac{2}{q\varepsilon_0\varepsilon_{CZTS}}\frac{V_{bi}-V}{N_A} \qquad (6)$$

The transit time (τ_T) was calculated by multiplying C$_3$ and R$_3$ of the equivalent circuit, and is represented vs the voltage (Fig. 9b) and characteristic values of both cells are showed in the *Table 3*. This measure can be associated with the minority carrier lifetime when it is measured in the area where the capacitance is dominated by the chemical capacitance. Apparently, reduction in the minority lifetime is affecting to the C$_{60}$/CdS due to mainly a reduction in the R$_3$, associated with the recombination resistance. However, the calculated values in both cases are much higher than the reported ones by other methods, and are in the order of few nanoseconds[44]. This discrepancy suggests that the carrier lifetime can change under illumination conditions due to changes in the carrier concentrations.

To check this effect for the CZTS/C$_{60}$/CdS device, the impedance spectra were also measured and compared under the light illumination near to V_{oc}, (700mV) and the equivalent bias voltage of 700 mV in dark (Fig. 11). It can be noted that the shape of semicircle decreases under illumination, due to decrease in the recombination resistance, and a drop of the capacitance. At this point, the carrier diffusion dominates, but the carrier lifetime decreases substantially to a value in the order of 1µs. This value is still much higher than the reported ones of ~20ns, pointing that the carrier lifetime measured close to the junction is not a limiting factor, but there are other processes that lowers this value within the bulk. In addition, a reduction in the series resistance (R$_1$) can be noticed under illumination from 185 to 45 Ω, which reaffirms that the C$_{60}$/CdS bilayer buffer is highly photoactive. This effect produces that the power extracted from a solar cell can be further increased with the illumination time. Measurements following the maximum power point under 1 sun illumination (Fig. S4) shows that during the first 30-40 s the observed power increase is mainly due to an increase in the extracted current, increasing the PCE from 4.4% to 4.6%.

Conclusions

The partial substitution of CdS by an organic charge transport materials is shown to be an effective method to reduce the loading of Cd based materials, without having adverse effect on the perfomance of the solar cells. We noted that reducing the thickness of CdS also induces an increase in photocurrent in the violet and UV region of the spectra, where the absorption of CdS is parasitic. The employed fullerene derivative as electron transport layer was noted to be stable under the required post treatment temperature of 230°C for fabrication of CZTSe solar cells. Among fullerene derivatives, C$_{60}$ showed better electro-optical properties than of C$_{70}$ as buffer layer in kesterites solar cell. The use of C$_{60}$ as an interlayer between the absorber and the CdS allowed to register remarkably high values of the V_{oc}, of 446 mV for CZTSe, and 718mV for CZTS, even with a significant reduction of the CdS thickness. For pure sulfide CZTS kesterite, the use of a double buffer of C$_{60}$ and CdS was noted to increase the carrier concentration close to the junction, and an increase in the built-in potential was responsible for the high V_{oc}. Optimization of the process and thicknes of these films will be

vital to further reduce the voltage deficit. One of the main barriers in inorganic solar cells is the limited choice of materials that can be used efficiently as buffer layers, and is being typically dependent on cadmium or indium elements and here rational organic charge transport materials can be employed. Our investigation paves the way for further optimization and exploration of employing organic materials for kesterite type solar cells to develop cost effective and green photovoltaics.

Conflicts of interest

There are no conflicts to declare.

Acknowledgements

References

1   S. Giraldo, Z. Jehl, M. Placidi, V. Izquierdo-Roca, A. Pérez-Rodríguez and E. Saucedo, *Adv. Mater.*, 2019, 1806692.

2   T. Todorov, H. W. Hillhouse, S. Aazou, Z. Sekkat, O. Vigil-Galán, S. D. Deshmukh, R. Agrawal, S. Bourdais, M. Valdés, P. Arnou, D. B. Mitzi and P. J. Dale, *J. Phys. Energy*, 2020, **2**, 012003.

3   L. H. Wong, A. Zakutayev, J. D. Major, X. Hao, A. Walsh, T. K. Todorov and E. Saucedo, *J. Phys. Energy*, 2019, **1**, 032001.

4   C. Platzer-Björkman, N. Barreau, M. Bär, L. Choubrac, L. Grenet, J. Heo, T. Kubart, A. Mittiga, Y. Sanchez, J. Scragg, S. Sinha and M. Valentini, *J. Phys. Energy*, 2019, **1**, 044005.

5   O. Vigil-Galán, F. A. A. Pulgarín, F. Cruz-Gandarilla, M. Courel, G. Villarreal-Ruiz, Y. Sánchez, D. Jiménez-Olarte and E. Saucedo, *Mater. Des.*, 2016, **99**, 254–261.

6   M. Neuschitzer, Y. Sanchez, S. Lopez-Marino, H. Xie, A. Fairbrother, M. Placidi, S. Haass, V. Izquierdo-Roca, A. Perez-Rodriguez and E. Saucedo, *Prog. Photovoltaics Res. Appl.*, 2015, **23**, 1660–1667.

7   M. Nguyen, K. Ernits, K. F. Tai, C. F. Ng, S. S. Pramana, W. A. Sasangka, S. K. Batabyal, T. Holopainen, D. Meissner, A. Neisser and L. H.Wong, *Sol. Energy*, 2015, **111**, 344–349.

8   A. Ghosh, R. Thangavel and A. Gupta, *J. Alloys Compd.*, 2017, **694**, 394–400.

9   M. Neuschitzer, K. Lienau, M. Guc, L. C. Barrio, S. Haass, J. M. Prieto, Y. Sanchez, M. Espindola-Rodriguez, Y. Romanyuk, A. Perez-Rodriguez, V. Izquierdo-Roca and E. Saucedo, *J. Phys. D. Appl. Phys.*, 2016, **49**, 125602.

10 D. A. R. Barkhouse, R. Haight, N. Sakai, H. Hiroi, H. Sugimoto and D. B. Mitzi, *Appl. Phys. Lett.*, 2012, **100**, 193904.

11 T. Ericson, F. Larsson, T. Törndahl, C. Frisk, J. Larsen, V. Kosyak, C. Hägglund, S. Li and C. Platzer-Björkman, *Sol. RRL*, 2017, **1**, 1700001.

12 K. Sun, C. Yan, F. Liu, J. Huang, F. Zhou, J. A. Stride, M. Green and X. Hao, *Adv. Energy Mater.*, 2016, **6**, 1600046.

13 H. Hiroi, J. Kim, M. Kuwahara, T. K. Todorov, D. Nair, M. Hopstaken, Y. Zhu, O. Gunawan, D. B. Mitzi and H. Sugimoto, in *2014 IEEE 40th Photovoltaic Specialist Conference, PVSC 2014*, IEEE, 2014, pp. 30–32.

14 H. W. Kroto, J. R. Heath, S. C. O'Brien, R. F. Curl and R. E. Smalley, *Nature*, 1985, **318**, 162–163.

15 N. S. Sariciftci, D. Braun, C. Zhang, V. I. Srdanov, A. J. Heeger, G. Stucky and F. Wudl, *Appl. Phys. Lett.*, 1993, **62**, 585–587.

16 M. Koltun, D. Faiman, S. Goren, E. A. Katz, E. Kunoff, A. Shames, S. Shtutina and B. Uzan, *Sol. Energy Mater. Sol. Cells*, 1996, **44**, 485–491.

17 C.-H. Chiang and C.-G. Wu, *Nat. Photonics*, 2016, **10**, 196–200.

18 K. Wojciechowski, T. Leijtens, S. Siprova, C. Schlueter, M. T. Hörantner, J. T. W. Wang, C. Z. Li, A. K. Y. Jen, T. L. Lee and H. J. Snaith, *J. Phys. Chem. Lett.*, 2015, **6**, 2399–2405.

19 C. Chen, S. Zhang, S. Wu, W. Zhang, H. Zhu, Z. Xiong, Y. Zhang and W. Chen, *RSC Adv.*, 2017, **7**, 35819–35826.

20 J.-J. Wang, J.-S. Hu, Y.-G. Guo and L.-J. Wan, *NPG Asia Mater.*, 2012, **4**, e2–e2.

21 S. J. Jang, N. T. Ho, M. H. Lee and Y. S. Kim, in *Journal of Physics: Conference Series*, IOP Publishing, 2017, vol. 864, p. 012065.

22 S. K. Saha, A. Guchhait and A. J. Pal, *Phys. Chem. Chem. Phys.*, 2012, **14**, 8090–8096.

23 K. Mokurala, L. L. Baranowski, F. W. de Souza Lucas, S. Siol, M. F. A M van Hest, S. Mallick, P. Bhargava and A. Zakutayev, , DOI:10.1021/acscombsci.6b00074.

24 V. Tunuguntla, W.-C. Chen, T. D. Newman, C.-Y. Chen, M.-C. Hsieh, S.-H. Lu, C. Su, L.-C. Chen and K.-H. Chen, , DOI:10.1016/j.solmat.2016.01.004.

25 T. Ericson, J. J. Scragg, A. Hultqvist, J. T. Watjen, P. Szaniawski, T. Torndahl and C. Platzer-Bjorkman, *IEEE J. Photovoltaics*, 2014, **4**, 465–469.

26 S. Kim, K. M. Kim, H. Tampo, H. Shibata and S. Niki, *Appl. Phys. Express*, 2016, **9**, 102301.

27 A. V. Shamardin, A. S. Opanasyuk, D. I. Kurbatov and M. E. Istratov, in *Proceedings of the 2017 IEEE 7th International Conference on Nanomaterials: Applications and Properties, NAP 2017*, Institute of Electrical and Electronics Engineers Inc., 2017, vol. 2017–January.

28 M. Neuschitzer, Y. Sanchez, S. Lõpez-Marino, H. Xie, A. Fairbrother, M. Placidi, S. Haass, V. Izquierdo-Roca, A. Perez-Rodriguez and E. Saucedo, *Prog. Photovoltaics Res. Appl.*, 2015, **23**, 1660–1667.

29 S. Lee, E. S. Lee, T. Y. Kim, J. S. Cho, Y. J. Eo, J. H. Yun and A. Cho, *Sol. Energy Mater. Sol. Cells*, 2015, **141**, 299–308.

30 M. A. Contreras, M. J. Romero, B. To, F. Hasoon, R. Noufi, S. Ward and K. Ramanathan, in *Thin Solid Films*, 2002, vol. 403–404, pp. 204–211.

31 L. Teng, J. Tong, G. Wang, L. Wang, L. Chen, S. Wang, Y. Wang, D. Pan, X. Zhang and Y. Liu, *J. Energy Chem.*, 2020, **42**, 77–82.

32 W.-C. Chen, C.-Y. Chen, Y.-R. Lin, J.-K. Chang, C.-H. Chen, Y.-P. Chiu, C.-I. Wu, K.-H. Chen and L.-C. Chen, *Mater. Today Energy*, 2019, **13**, 256–266.

33 V. I. Zubov, N. P. Tretiakov, J. N. Teixeira Rabelo and J. F. Sanchez Ortiz, *Phys. Lett. A*, 1994, **194**, 223–227.

34 H. S. Lin, I. Jeon, R. Xiang, S. Seo, J. W. Lee, C. Li, A. Pal, S. Manzhos, M. S. Goorsky, Y. Yang, S. Maruyama and Y. Matsuo, *ACS Appl. Mater. Interfaces*, 2018, **10**, 39590–39598.

35 M. Bär, B. A. Schubert, B. Marsen, R. G. Wilks, S. Pookpanratana, M. Blum, S. Krause, T. Unold, W. Yang, L. Weinhardt, C. Heske and H. W. Schock, *Appl. Phys. Lett.*, 2011, **99**, 222105.

36 A. Fairbrother, E. García-Hemme, V. Izquierdo-Roca, X. Fontané, F. A. Pulgarín-Agudelo, O. Vigil-Galán, A. Pérez-Rodríguez and E. Saucedo, *J. Am. Chem. Soc.*, 2012, **134**, 8018–8021.

37   H. Sun, K. Sun, J. Huang, C. Yan, F. Liu, J. Park, A. Pu, J. A. Stride, M. A. Green and X. Hao, *ACS Appl. Energy Mater.*, 2018, **1**, 154–160.

38   H. Xie, Y. Sáncheza, P. Tang, M. Espíndola-Rodríguez, M. Guc, L. Calvo-Barrio, S. López-Marino, Y. Liu, J. R. Morante, A. Cabot, V. Izquierdo-Roca, J. Arbiol, A. Pérez-Rodríguez and E. Saucedo, *Sol. RRL*, 2018, **3**, 1800279.

39   C. Yan, J. Huang, K. Sun, S. Johnston, Y. Zhang, H. Sun, A. Pu, M. He, F. Liu, K. Eder, L. Yang, J. M. Cairney, N. J. Ekins-Daukes, Z. Hameiri, J. A. Stride, S. Chen, M. A. Green and X. Hao, *Nat. Energy*, 2018, **3**, 764–772.

40   P. A. Fernandes, P. M. P. Salomé, A. F. Sartori, J. Malaquias, A. F. Da Cunha, B. A. Schubert, J. C. González and G. M. Ribeiro, *Sol. Energy Mater. Sol. Cells*, 2013, **115**, 157–165.

41   G. K. Gupta, A. Garg and A. Dixit, *J. Appl. Phys.*, , DOI:10.1063/1.5002619.

42   I. Mora-Seró, G. Garcia-Belmonte, P. P. Boix, M. A. Vázquez and J. Bisquert, *Energy Environ. Sci.*, 2009, **2**, 678–686.

43   C. Yan, F. Liu, K. Sun, N. Song, J. A. Stride, F. Zhou, X. Hao and M. Green, *Sol. Energy Mater. Sol. Cells*, 2016, **144**, 700–706.

44   K. Sun, C. Yan, J. Huang, K. Sun, H. Sun, L. Jiang, X. Deng, J. Stride, X. Hao and F. Liu, *J. Alloys Compd.*, 2018, **750**, 328–332.